



HAL
open science

Determination of residual stress gradient in a Ti-stabilized austenitic stainless steel cladding candidate after carburization in liquid sodium at 500 °C and 600 °C

Mohamed Fares Slim, Guillaume Geandier, Fabien Rouillard, Benoît Malard

► To cite this version:

Mohamed Fares Slim, Guillaume Geandier, Fabien Rouillard, Benoît Malard. Determination of residual stress gradient in a Ti-stabilized austenitic stainless steel cladding candidate after carburization in liquid sodium at 500 °C and 600 °C. *Acta Materialia*, 2021, 221, pp.117435. 10.1016/j.actamat.2021.117435 . hal-03588958

HAL Id: hal-03588958

<https://hal.science/hal-03588958>

Submitted on 25 Feb 2022

HAL is a multi-disciplinary open access archive for the deposit and dissemination of scientific research documents, whether they are published or not. The documents may come from teaching and research institutions in France or abroad, or from public or private research centers.

L'archive ouverte pluridisciplinaire **HAL**, est destinée au dépôt et à la diffusion de documents scientifiques de niveau recherche, publiés ou non, émanant des établissements d'enseignement et de recherche français ou étrangers, des laboratoires publics ou privés.



Distributed under a Creative Commons Attribution - NonCommercial - NoDerivatives 4.0 International License




Open Archive Toulouse Archive Ouverte (OATAO)

OATAO is an open access repository that collects the work of Toulouse researchers and makes it freely available over the web where possible

This is an author's version published in: <http://oatao.univ-toulouse.fr/28774>

Official URL: <https://doi.org/10.1016/j.actamat.2021.117435>

To cite this version:

Slim, Mohamed Fares and Geandier, Guillaume and Rouillard, Fabien and Malard, Benoît  *Determination of residual stress gradient in a Ti-stabilized austenitic stainless steel cladding candidate after carburization in liquid sodium at 500 °C and 600 °C.* (2021) Acta Materialia, 221. 117435. ISSN 1359-6454

Any correspondence concerning this service should be sent to the repository administrator: tech-oatao@listes-diff.inp-toulouse.fr

Determination of residual stress gradient in a Ti-stabilized austenitic stainless steel cladding candidate after carburization in liquid sodium at 500 °C and 600 °C

Mohamed Fares Slim^{a,b,*}, Guillaume Geandier^a, Fabien Rouillard^c, Benoit Malard^d

^a Université de Lorraine, CNRS, IJL, F - 54000, France

^b ESRF – The European Synchrotron, 71 Avenue des Martyrs, 38000 Grenoble, France

^c Université Paris-Saclay, CEA, Service de la Corrosion et du Comportement des Matériaux dans leur Environnement, 91191, Gif-sur-Yvette, France

^d CIRIMAT, Université de Toulouse, CNRS, INPT, UPS, 4 allée Émile Monso, 31030 Toulouse, France

ARTICLE INFO

Keywords:

Residual stress

High energy X-ray diffraction

Carburization

Expanded austenite

Carbide precipitation

Nuclear liquid sodium

ABSTRACT

Non-destructive residual stress profile measurement with a micrometric depth resolution within the depth of carburized Ti-stabilized stainless steel cladding candidate was carried out by high-energy X-ray diffraction. The samples were carburized in carburizing nuclear liquid sodium at 500 °C and 600 °C for 1000 h. The full residual stress tensor profile was determined thanks to the estimation of the strain-free lattice parameter evolution using the carbon concentration profile measured by electron probe microanalysis and thermodynamic simulation. For the sample carburized at 500 °C, the residual stress genesis was governed by the carbon concentration within the steel and the formation of expanded austenite. For the sample carburized at 600 °C, the residual stress profile in the austenitic matrix depended on the precipitation of $M_{23}C_6$ carbide. Stress relaxation was observed in the intragranular carburization zone. For the two temperatures, compressive residual stresses developed in the carburized zone and tensile stresses developed in the rest of the sample.

1. Introduction

As an alternative for the third-generation of nuclear reactors, the French alternative energies and atomic energy commission (CEA) has launched the development of a new generation of sodium-cooled fast nuclear reactor (SFR). As a part of this development, many research programs have been started on the different SFR reactor components. This paper focused on the long-term performance of the control rods cladding which are located in the core of the reactor. Feedbacks from first tests in former French experimental sodium fast reactors evidenced the premature rupture of this cladding. From the expertise of the broken cladding, it has been evidenced that the carburization of the stainless steel cladding was the main cause of failure. It is well known that the mechanical properties of steels such as the ductility or the fracture strain are reduced after carburization [1–3]. The carburization of stainless steel after exposure to nuclear grade liquid sodium containing carbon was extensively studied in the past [4, 5] and more recently [6–9]. Ti-stabilized austenitic stainless steel AIM1, a stainless steel cladding candidate for control rods, formed a carburized

zone after 1000 h of exposure in carburizing liquid sodium at temperatures of 500 °C and 600 °C [8, 9]. Carbon diffuses into the steel and, depending on the temperature, oversaturates the austenitic matrix and/or forms carbides. The effect of the carburization profile characterized, among others, by the maximum carburization depth or the fraction of carbides, on the ductility, has been studied in detail at room and high temperature [3]. Another important mechanical consequence of carburization is the generation of residual stress profiles induced mainly by a gradient of composition in the matrix and the formation of new phases (mainly carbides) [10]. The residual stresses profiles are often determined from thermo-mechanical simulation because experimental access to them is not easy. The brightness and high photon flux available nowadays at synchrotron sources allow to work with a highly collimated X-ray beam and reach nanometric resolution. The ability of such technique to resolve depth gradients of microstructure and residual stress were demonstrated in the past [11–15].

The goal of this study was to determine, with a micrometric resolution, the full residual stress tensor in the sample depth of Ti-stabilized austenitic stainless steel carburized in sodium in the operating temperature range of control rods, between 500 and 600 °C. In that purpose, the effect of composition on the lattice parameter of austenite and carbides (called “strain-free” lattice pa-

* Corresponding author.

E-mail address: mohamed-fares.slim@esrf.fr (M.F. Slim).

Table 1
Composition of the AIM1 austenitic stainless steel (wt.%) analyzed by inductively coupled plasma-optical emission spectrometry (ICP-OES) and combustion analysis for carbon.

Cr	Ni	Mo	C	Ti	Mn	Co	Si	Cu	Al	Fe
14.35	14.05	1.40	0.09	0.36	1.40	0.02	0.73	0.12	0.015	Base

parameter) is needed to take into account the “chemical” effect on the lattice parameter values measured by X-ray diffraction. This “chemical” effect on the lattice parameter is not, often, easily accessible and, in consequence, not always considered for the determination of residual stress profiles published in literature. Nevertheless, this effect can be strong and thus should always be considered rigorously. In this study, the chemical composition of the different phases was first obtained through the measurement of carbon profile by EPMA and thermodynamic simulations. Then, the effect of the composition gradient on the lattice parameter of austenite and carbides was predicted from empirical laws given in literature. Finally, the residual stress profiles could be determined from the evolution of the non-chemically induced lattice parameter values by high energy X-ray diffraction. The obtained residual stress profiles were discussed at the light of the developed microstructures.

2. Experimental details

2.1. Material and carburization experiments

The studied material was a Ti-stabilized austenitic stainless steel AIM1 quenched at 1130 °C and strain-hardened during rolling to 25%. The detailed chemical composition of the studied steel is given in Table 1. At initial state, the AIM1 alloy was composed of austenite and a small quantity of TiC carbide (about 1 to 2 wt.%). The grains were mostly equiaxed with an average size of 40 µm.

AIM1 austenitic stainless steel samples were carburized at 500 °C and 600 °C for 1000 h. The carburization experiments were performed in a mild steel crucible (iron containing 0.38 wt.% of carbon) filled with around two liters of nuclear grade liquid sodium and containing additional mild steel plates. These mild steel plates were added in order to maintain a high carbon activity in sodium during the whole test duration. Before exposing to sodium, the AIM1 samples of dimensions 20 × 20 × 1 mm³ were cleaned in ethanol and the liquid sodium was purified from dissolved oxygen using zirconium foil at 600 °C for three days (to obtain an oxygen concentration lower than 5 ppm). More details on the procedure for carburization experiments in sodium can be found in previous works of Romedenne et al. [8, 16, 17]. After carburization, samples with dimensions of 3 × 3 × 1 mm³ were cut from the middle of the carburized plates and used for the different experimental characterizations. A non-carburized sample was annealed in helium at 600 °C for 1000 h in order to remove any residual stresses induced by rolling. It was used as an unstressed sample reference in this study.

2.2. High-energy X-ray diffraction experiment

The reference and carburized samples were characterized by HEXRD in transmission mode at the PETRA P07-EH2 beamline (DESY-Petra III, Hamburg, Germany). A schematic presentation of the experimental set-up is given in Fig. 1a. The high-energy monochromatic rectangle-shaped beam with specific dimensions of 300 µm in length and 2 µm in height, see Fig. 1b, ($E = 103.4$ keV, $\lambda = 0.119907$ Å) allowed working in transmission on the cross-section of the sample of dimensions 3 × 3 × 1 mm³ (3 mm in the S_1 and S_2 directions and 1 mm in the S_3 direction,

see Fig. 1b). The sample was animated by a translational movement along the S_3 axis with a velocity $V = 10$ µm/s. A 2D Perkin Elmer detector (2048 × 2048 pixels, pixel size of 200 × 200 µm²) with a high acquisition rate (10 Hz) placed at 1.5 m from the sample was used to record the whole Debye-Scherrer rings with a maximum 2θ angle of 7.5°. The continuous translational movement of the sample along the S_3 axis coupled with the high image acquisition rate of the 2D detector allowed recording 2D images of a diffracted volume of 300 × 3000 × 3 µm³ at every micrometer through all the traveled thickness (from the surface of the sample up to 500 µm in depth). In order to center the specimen and align its upper surface to be parallel to the beam, series of absorption and reflective scans using the direct beam and a photodiode positioned behind the sample were carried out. Considering the high photon energy and the resulting small scattering angles, the alignment had to be carried out at high precision thanks to three translations and rotations. No assumption on the stress state in the plane of the samples (S_1, S_2) was taken. In consequence, 2D images were acquired at three different χ orientations: 0°, 90° and -90° around the S_3 axis. The ω rotation was set equal to zero during the experiments.

3. Data treatment

3.1. Phases mass fractions

The 2D diffraction images recorded during the experiments were integrated all around the rings using PyFAI software [18]. The 2D detector to sample distance and the detector tilts were calibrated using a cerium dioxide powder diffraction standard from NIST (CeO₂ – SRM 674b). The obtained 1D diffractograms (Intensity vs 2θ) were corrected from the instrumental contribution, using the same powder diffraction standard, and analyzed with a full Rietveld refinement procedure using MAUD software (Material Analysis Using Diffraction) [19]. After data processing, the Rietveld refinement allowed to determine the evolution of the mass fractions of the phases present in the alloy. The absolute uncertainties on the measured mass fraction was 2 wt.%. The carbides mass fractions determined by Rietveld analysis allowed the calculation of the carbon mass fraction trapped in carbides using Eq. 1:

$$w_c^{\text{Carbides}}(\text{wt. \%}) = f^{M_{23}C_6} \cdot w_c^{M_{23}C_6} + f^{M_7C_3} \cdot w_c^{M_7C_3} + f^{\text{TiC}} \cdot w_c^{\text{TiC}} \quad (1)$$

with f^x the mass fraction of the phase X and w_c^x the carbon mass fraction in the phase X.

3.2. Residual stress determination

X-ray diffraction is a selective experimental technique. It allows strain/stress measurement in each phase within a multiphased material by comparing the variation of interplanar distance of a crystallographic plane to a reference value. This reference value must be determined from an unstressed sample with the same chemical composition. More details on the determination of this value is given later in the paper. In the case of a single-phase material, the strain/stress measured within the phase is equal to the macroscopic stress in the sample. However, in the case of a multiphased material such as in carburized steel, the macroscopic stress in the sample is the sum of the stress created in all phases weighted by their volume fractions in the material (see Eq. (8)).

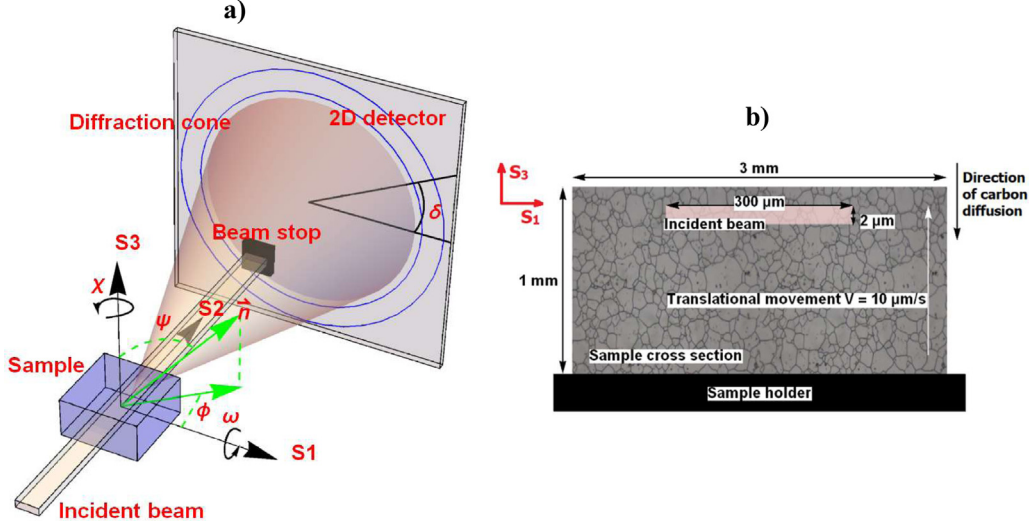


Fig. 1. a) Experimental set-up of the HEXRD measurements, b) Schematic view (not to scale) of the sample cross-section.

The stress analysis was performed by applying the $\sin^2\Psi$ method. After the calibration procedure made on a cerium dioxide powder diffraction standard (CeO₂-SRM 674b), the recorded 2D diffraction images were integrated around the azimuthal angle δ along the Debye-Scherrer ring over 2° sectors using pyFAI software [18]. In order to determine the residual stresses in the alloy, the variation of the inter planar distance d_{hkl} in different directions should be determined. So, at least the directions dependent positions 2Θ of one plane of each phase must be evaluated. The austenite (γ_{Fe}) (220) and $M_{23}C_6$ (420) peaks were selected as they do not overlap with peaks of other phases. In the zone where M_7C_3 precipitated, no residual stress determination was carried out because the peaks of M_7C_3 overlapped with peaks of other phases (austenite and $M_{23}C_6$ mainly). The mechanical effect of TiC carbide was neglected as its mass fraction does not exceed 2%, see § 4.1. The peaks line profiles were fitted using a Pearson VII function. An automatic procedure was developed using Python environment to analyze the data. After data processing, 2Θ positions, full width at half maximum (FWHM), intensity, shape factor, background parameters and residual stresses were extracted. The FWHM is sensitive to stress-strain accumulation (dislocation density), microstrains (strain heterogeneities between and inside grains) and microstructural evolution (essentially chemical gradient in our case). In order to consider the uncertainties in the 2Θ position due to the variations of the beam position during experiments and to free ourselves of the exact knowledge of the Debye-Scherer ring center, an average 2Θ position for the opposite azimuths (δ and $\delta + 180^\circ$) was used in the residual stress determination [20, 21].

In the case of a triaxial residual stress state, assuming a macroscopically elastically isotropic behavior of the material and assuming that the chemical gradient has a negligible effect on the material elasticity constants, the strain in the measurement direction $\varepsilon_{\Phi\Psi}$ can be written as following [22, 23]:

$$\varepsilon_{\Phi\Psi} = \ln\left(\frac{\sin\theta_0^{hkl}}{\sin\theta^{hkl}}\right) = \frac{1}{2}S_2^{hkl}(\sigma_\Phi - \sigma_{33})\sin^2\Psi + \frac{1}{2}S_2^{hkl}\tau_\Phi \sin(2\Psi) + \frac{1}{2}S_2^{hkl}\sigma_{33} + S_1^{hkl}Tr(\bar{\sigma}) \quad (2)$$

$$\sigma_\Phi = \sigma_{11}\cos^2\Phi + \sigma_{12}\sin 2\Phi + \sigma_{22}\sin^2\Phi \quad (3)$$

$$\tau_\Phi = \sigma_{13}\cos\Phi + \sigma_{23}\sin\Phi \quad (4)$$

Table 2
XEC of austenite (220) and $M_{23}C_6$ (420) calculated from literature data using Hill model.

	$\frac{1}{2}S_2$ (10^{-6} MPa ⁻¹)	S_1 (10^{-6} MPa ⁻¹)
Austenite (γ_{Fe}) (220)	6.47	- 1.44
$M_{23}C_6$ (420)	3.627	- 0.817

$$Tr(\bar{\sigma}) = \sigma_{11} + \sigma_{22} + \sigma_{33} \quad (5)$$

with S_1^{hkl} and $\frac{1}{2}S_2^{hkl}$ the X-ray elasticity constants (XEC) of plane (hkl), θ_0^{hkl} the strain-free diffraction angle of the diffracting plane and θ^{hkl} the diffraction angle of the stressed plane, $\bar{\sigma}$ the stress tensor and σ_{ij} and ε_{ij} the stress and strain tensors components respectively. In the case of a triaxial stress state, by plotting $\varepsilon_{\Phi\Psi}$ as function of $\sin^2\Psi$, an ellipse is obtained. The slope of the ellipse axis presents the stress difference in the plane of measurement and the ellipse opening allows to determine the shear stresses. In our case, the $\sin^2\Psi$ curves were almost linear and no ellipse was observed meaning that no shear stresses (or negligible) were developed after carburization. In the following, only the σ_{ii} components were presented since the σ_{ij} , with $i \neq j$ components were negligible. The transformation of angles δ (azimuthal angle along the Debye-Scherrer ring), χ (sample rotation around its normal; S_3 axis) and ω (sample rotation around S_1 axis) into classical angles Φ and Ψ defining the measurement direction \vec{n} (see Fig. 1a) was done using the formulas given in the literature [21, 24, 25].

The XEC of the γ_{Fe} (220) and $M_{23}C_6$ (420) were calculated from the single-crystal elasticity constants found in literature [26, 27] using Hill model [28] and are presented in Table 2. The dependence of austenite and $M_{23}C_6$ XECs on the chemical depth gradient was not considered. It will be discussed later in § 5.1.2 and § 5.2.3. The uncertainties on the residual stresses were calculated using the uncertainty propagation equation based on the methodology referenced in the metrology documents [29, 30]. Its main source was the uncertainty committed on the calculated stress-free lattice parameter.

From Eq. (2) it is possible to extract the full residual stress tensor if the strain-free diffraction angle of the diffracting plane, i.e. the strain-free lattice parameter, is known. Usually, the strain-free lattice parameter can be determined through various methodologies: by using a powder of the same material, by long time annealing of the sample or by sectioning the sample in small pieces

in order to relax the macroscopic residual stress developed in the specimen. More details can be found elsewhere [31]. First, the carburized samples studied in this paper have a steep gradient of composition and microstructure with respect to the sample depth which makes the production of a powder with the same characteristic practically impossible. Then, annealing the sample could induce microstructure change of the sample such as the precipitation and coarsening of carbides and/or the decomposition of expanded austenite. Finally, sample sectioning in our case is very difficult, expensive and time consuming and the results are not guaranteed as coupons of a few micrometers have to be produced and measured. In this study, the strain-free lattice parameters of austenite and $M_{23}C_6$ were determined from an empirical relationship giving the strain-free lattice parameters of both phases as a function of their compositions. More details will be given in the following sections and can also be found in a previous work [9].

3.2.1. Methodology of the determination of the strain-free lattice parameter of austenite and $M_{23}C_6$ carbide

The austenite strain-free lattice parameter, $a_{\gamma}^{\text{strain-free}}$, was calculated using an empirical model extracted from literature [32]. The model describes the evolution of the lattice parameter of austenite as a function of the concentration of carbon and of all the alloying elements present in austenite (Eq. (6)).

$$\begin{aligned} a_{\gamma}^{\text{strain-free}} = & a_0 + \alpha_C \times \%C^{\gamma} + 0.0006(\pm 0.0003) \times \%Cr^{\gamma} \\ & + 0.00095(\pm 0.00015) \times \%Mn^{\gamma} - 0.0002(\pm 0.00004) \\ & \times \%Ni^{\gamma} + 0.0056(\pm 0.0007) \times \%Al^{\gamma} - 0.0004(\pm 0.0001) \\ & \times \%Co^{\gamma} + 0.0015(\pm 0.0005) \times \%Cu^{\gamma} + 0.0031(\pm 0.0004) \\ & \times \%Mo^{\gamma} + 0.0039(\pm 0.0009) \times \%Ti^{\gamma} \end{aligned} \quad (6)$$

In Eq. (6), a_0 is the lattice parameter of austenite at ambient temperature in absence of any alloying elements, α_M is the lattice expansion coefficient of the metallic element M and $\%M^{\gamma}$ is the wt.% of the element M in austenite. In this work, a_0 was obtained by subtracting the lattice expansion caused by the dissolved carbon and the alloying elements M present in the austenitic matrix in the as-received steel (calculated by ThermoCalc® using the steel composition given in Table 1), from the initial lattice parameter ($a_{\gamma}^{\text{initial}}$) of AIM1 alloy. This last value was determined experimentally by HEXRD on the annealed sample at 600 °C in helium for 1000 h: $a_{\gamma}^{\text{initial}} = 3.5890 \pm 0.0005$ Å. The lattice expansion coefficients α_M of the alloying elements were taken from the work of Dyson and Holmes [32] which was the only complete work found in literature on this topic. According to literature, the lattice expansion coefficient of carbon α_C varies between 0.028 and 0.054 Å / (wt.%) C [32–40]. The multiple α_C values found in literature are due to two principal reasons: i) a few coefficients were determined on stressed samples which results on an incorrect value biased by stress effect and ii) the α_C values are determined for alloys having different compositions. In front of the difficulty to choose the right α_C value among all proposed values in literature, the lattice expansion coefficient value of carbon used in (Eq. (6)), α_C , was determined so that the macroscopic stress profile through the sample exposed at 500 °C for 1000 h was balanced (see § 5.1.1). This verification could only be done for the sample exposed at 500 °C since the residual stress determined in austenite for this specific sample could be considered as macroscopic as well. Indeed, this sample contained almost exclusively austenite (single phase). The presence of a thin $M_{23}C_6$ carbides rich layer near the very near surface (Fig. 2) was neglected. More details on the determination of α_C and the strain-free lattice parameters for the two temperatures, 500 °C and 600 °C, are given in sections 5.1 and 5.2.

The strain-free lattice parameter of $M_{23}C_6$ was calculated using Eq. 7. In Eq. 7, $w_X^{M_{23}C_6}$ represents the mass fraction of the element X in $M_{23}C_6$ carbide determined by Thermo-Calc®, $a^{Cr_{23}C_6}$ is

the $Cr_{23}C_6$ lattice parameter and $a^{(X, Cr)_{23}C_6}$ is the lattice parameter from the literature corresponding to the mass fraction of X in $M_{23}C_6$ [41]. $A = 0.108$ Å is a correction term applied to the data of Yi et al. [41] and represents the difference between the $Cr_{23}C_6$ lattice parameters measured by Bowman et al. [42] and calculated by Yi et al. [41]. The used data are showed in Figure 2 in supplementary materials.

$$\begin{aligned} a^{M_{23}C_6} = & w_{Mo}^{M_{23}C_6} \cdot a^{(Mo, Cr)_{23}C_6} + w_{Fe}^{M_{23}C_6} \cdot a^{(Fe, Cr)_{23}C_6} \\ & + (1 - w_{Mo}^{M_{23}C_6} - w_{Fe}^{M_{23}C_6}) \cdot a^{Cr_{23}C_6} + A \end{aligned} \quad (7)$$

3.2.2. Electron probe microanalysis experiment

The carbon concentration profiles within the depth of the samples were measured using an SX 100 CAMECA electron probe microanalyzer (EPMA) operated at 15 kV and 20 nA using the phi-rho-z method. The analytical crystal for K_{α} C was LPC2. To get a representative average carbon profile of the carbon contained both in substrate grains and grain boundaries, four surface profiles of $2 \times 50 \mu m^2$ were averaged. The profiles were conducted up to mid-thickness of the sample, i.e. 500 μm . More details on the measurement procedure are available in previous works [8, 16, 17].

4. Experimental results

4.1. Phases mass fractions

Fig. 2 and Fig. 3 show the evolution of the phases mass fractions measured by HEXRD respectively in AIM1 alloys carburized at 500 °C and 600 °C for 1000 h. TiC carbides were initially present in the alloy before carburization and its mass fraction did not evolve after carburization at a detectable level for HEXRD for the two carburization temperatures. At 500 °C, only $M_{23}C_6$ carbides were identified at the extreme surface of the sample (up to 6 μm in depth). In the case of carburization at 600 °C, $M_{23}C_6$ and M_7C_3 carbides were mainly formed in the sample. $M_{23}C_6$ carbides were present in the whole thickness of the sample with non-negligible quantity, ≥ 2 wt.% until 350 μm . M_7C_3 carbides were only detected within the first 60 μm below the sample surface. For more information about the formation of carbides, expanded austenite and phases distribution within the samples as a function of the carburization temperatures the reader can refer to previous works [8, 9].

4.2. Carbon concentration profile

Fig. 4 and Fig. 5 show a comparison between the carbon profile determined by EPMA and the carbon profile determined from the mass fraction of carbides detected by HEXRD in the AIM1 carburized respectively at 500 °C and 600 °C for 1000 h. At 500 °C (Fig. 4), the carbon concentration revealed by EPMA was much higher than the one calculated from the amount of carbides meaning that almost all carbon absorbed by the sample was not trapped into carbides. The carbon concentration reached at any depth was much higher than the solubility limit of carbon at 500 °C given by Thermo-Calc® (0.006 wt.%). Thus, a carbon supersaturation of the austenite matrix occurred: expanded austenite formed in the carburized zone [9]. This phenomenon has been previously evidenced by different authors in highly carburizing gaseous environments on low alloyed steels and stainless steels at temperatures under 550 °C [33, 34, 43–45] and in carburizing sodium at 500 °C [17]. At 600 °C (Fig. 5), both profiles are in excellent agreement. Since Eq. (1) considers only the carbon contained in carbides, this excellent agreement demonstrates that carbon which diffused within the sample was mainly trapped into carbides as expected by thermodynamic equilibrium. The formation of carbides resulted in metallic depletion of the austenite, mainly in chromium and molybdenum, two strong carbide former elements [9].

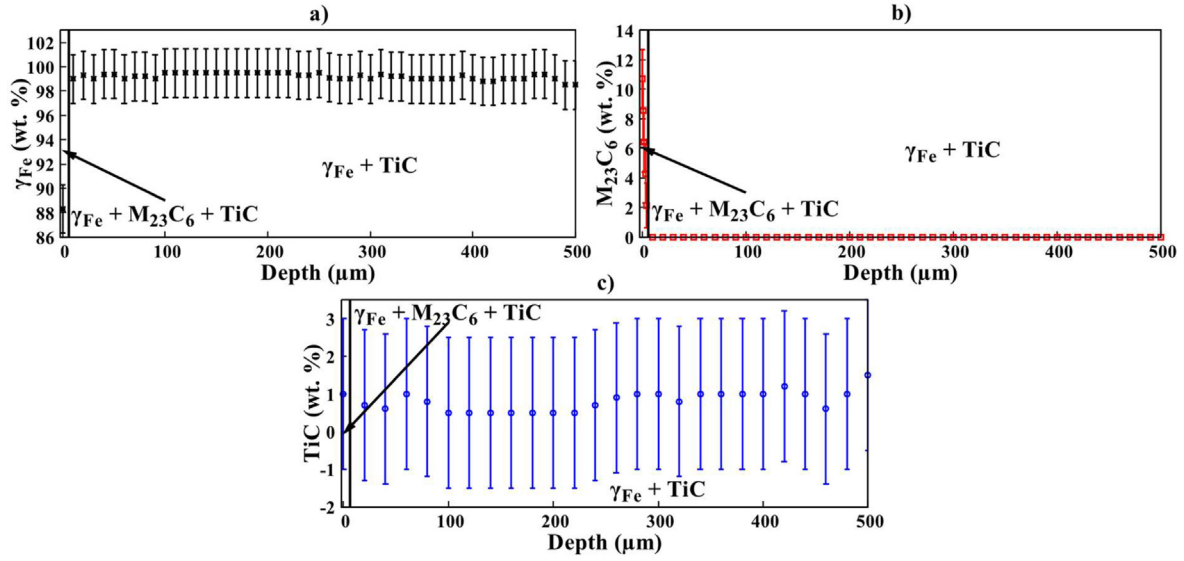


Fig. 2. Evolution of the phases mass fractions in AIM1 alloy carburized at 500 °C for 1000 h: a) austenite, b) $M_{23}C_6$ carbides, c) TiC carbides.

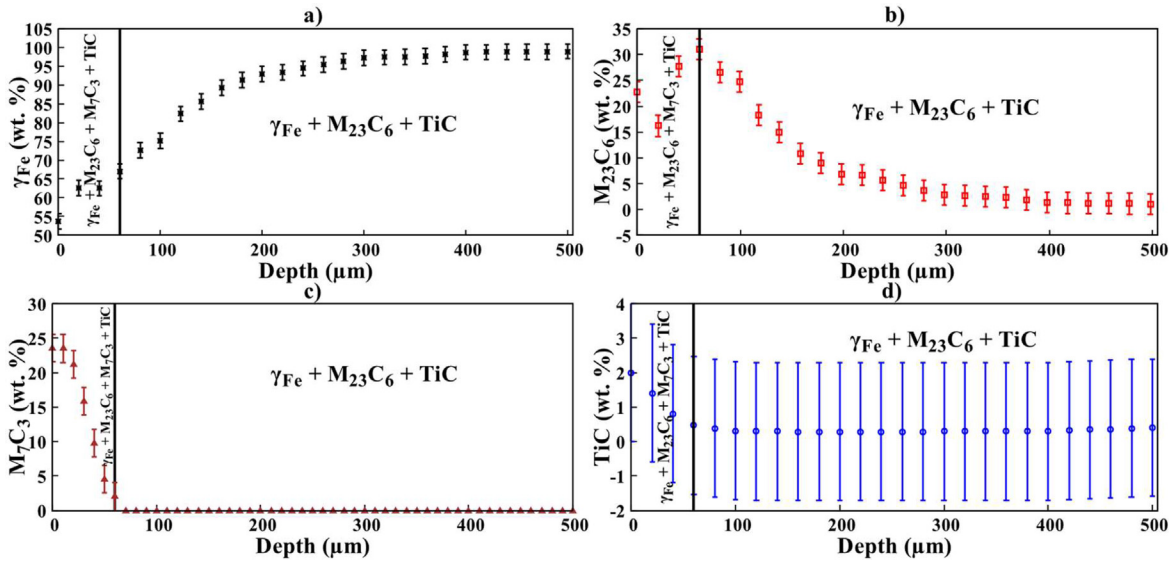


Fig. 3. Evolution of the phases mass fractions in AIM1 alloy carburized at 600 °C for 1000 h: a) austenite, b) $M_{23}C_6$ carbides, c) M_7C_3 carbides, d) TiC carbides.

5. Residual stress results and discussions

5.1. AIM1 alloy carburized at 500 °C for 1000 h

5.1.1. Strain-free lattice parameter of austenite

The strain-free lattice parameter for the sample carburized at 500 °C was determined as following:

- in the region where only carbon supersaturation of austenite occurred (no formation of carbides): the strain-free lattice parameter was determined using the EPMA carbon profile and the mass fraction of the metallic elements shown in Table 1.
- in the very thin region near the surface where $M_{23}C_6$ carbide formed: The chromium concentration in austenite was calculated using the measured mass fraction of $M_{23}C_6$ by HEXRD, considering that $M_{23}C_6$ contained only chromium as metallic component which is a rather good approximation if one considers Thermo-Calc® calculations. The carbon concentration in austenite was calculated as the difference between the carbon

concentrations measured by EPMA and the carbon contained in carbides and determined by HEXRD (calculated using Eq. (1)).

The optimum α_C coefficient, which satisfied the stress balance in the sample was found equal to $0.0405 \text{ \AA} / (\text{wt. \%}) \text{ C} (\pm 0.011)$. This value was within the range of the values proposed in literature (between 0.028 and $0.054 \text{ \AA} / (\text{wt. \%}) \text{ C}$, see section 3.2.1). The strain-free lattice parameter profile is shown in Fig. 6 and the residual stress profile is presented in the next section. In accordance with the carbon concentration profile (Fig. 4), an increase of the austenite lattice was observed in the carburized zone.

5.1.2. Residual stress profile

Fig. 7a, b, c and d show the evolution of the normal residual stress components, the von Mises stress (calculated using the von Mises yield criterion), the carbon concentration profile and the FWHM of austenite in AIM1 alloy carburized at 500 °C for 1000 h respectively. An equibiaxial stress state ($\sigma_{11} = \sigma_{22}$) was observed in the sample surface plane (S_1, S_2). In order to describe and dis-

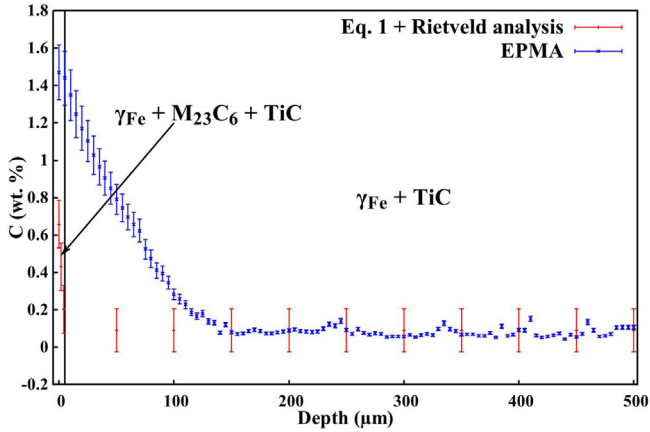


Fig. 4. Comparison between the carbon profiles in AIM1 carburized at 500 °C for 1000 h determined by EPMA and using Eq. 1.

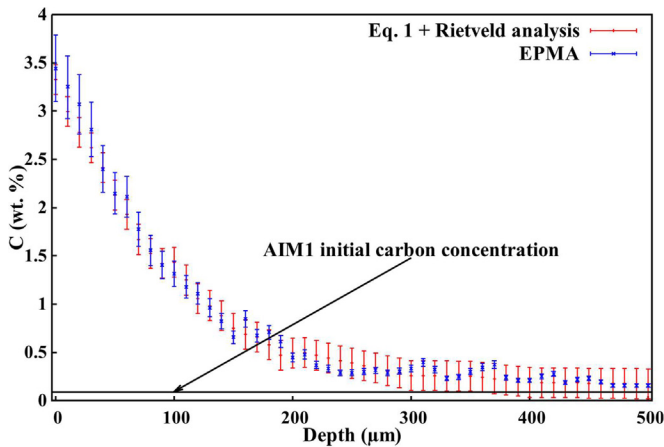


Fig. 5. Comparison between the carbon profiles in AIM1 carburized at 600 °C for 1000 h determined by EPMA and using Eq. 1.

cuss the observed stress profile, the investigated depth was divided into two regions.

- Region I: This is the carburized region, see Fig. 7c. Compressive residual stresses were developed in that zone, see Fig. 7a. A stress relaxation was observed at the surface of the sample due to free surface and, likely, the formation of carbides. Between 12 and 90 μm, the calculated von Mises stresses were higher than the tensile yield stress of as-received AIM1 alloy ($\sigma_y = 690$ MPa). This last parameter was measured indepen-

dently from tensile tests at room temperature [3]. The FWHM increased moderately between 90 and 30 μm (from 0.03 ° to 0.04 °) then sharply from 30 μm of depth to reach 0.1 ° near the sample surface, at 6 μm. A decrease of the FWHM was observed from 6 μm of depth going up to the sample surface. Nevertheless, it stayed higher than the value measured in the core of the material.

- Region II: This is the non-carburized region. In this region, a transition from compressive to tensile residual stress in the matrix was observed (Fig. 7a). The von Mises stresses were lower than the tensile yield stress of as-received AIM1 alloy (Fig. 7b). The carbon concentration was constant and equal to the AIM1 initial carbon concentration (Fig. 7c). The FWHM was also constant (Fig. 7d).

The formation of compressive residual stresses at the sample surface owing to the growth of expanded austenite, by carburization or nitridation, was extensively reported in the past [44–49]. In literature, the studied carburized samples were monophasic, contained expanded austenite in the carburized zone and austenite in the core, and the stresses were measured in the near sample surface in almost cases. Thus, a null stress perpendicular to the sample surface, $\sigma_{33} = 0$, was assumed. In our study, at the extreme surface, carbides were present with austenite. Thus, there was a multiphased material at the extreme surface of the sample. In this case, a non-null stress perpendicular to the sample surface is expected to occur [50] in agreement with the residual stress result showed in Fig. 7a. The development of compressive residual stress in the carburized zone can be explained as following. The carbon which diffused within the sample depth was almost entirely dissolved in the austenite matrix. Therefore, an expansion of the austenite lattice occurred at the sample surface (Fig. 6) [9]. The carburized zone, containing expanded austenite, was mechanically constrained by a non-carburized zone lying below the carburized region and containing as-received austenite. So, the expansion which was caused in the surface layer was restricted by the subsurface layer and resulted in compressing the surface region (carburized zone). Plastic deformation occurred in the region where $\sigma_{\text{von Mises}}$ were higher than tensile yield stress of the alloy. As mentioned in section 3.2, the FWHM evolution is proportional to different phenomena. At sample depth between the sample surface and 90 μm, plastic strains and chemical gradient were present. That may explain the FWHM increase observed in that zone. The presence of plastic strain in all points of that region cannot be confirmed or denied as the evolution of the yield stress of the studied steel as function of carbon concentration was not investigated. For example, Jiang et al. [51] have studied the mechanical properties gradient of a low temperature carburized 316 L stainless steel and have reported an enhancement of the yield stress as function of

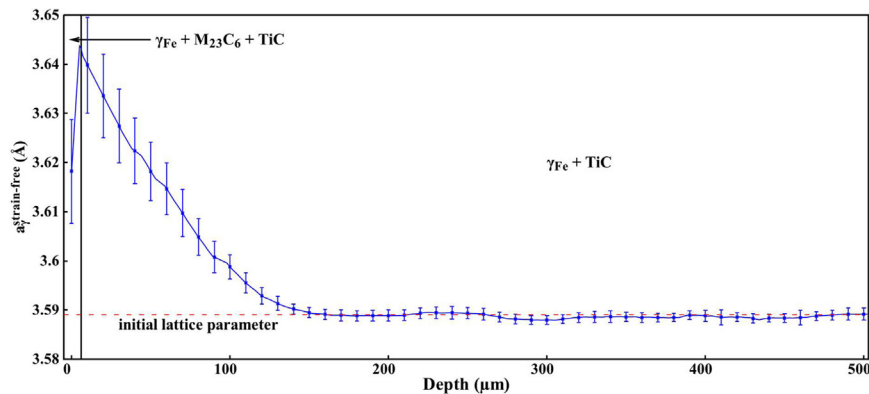


Fig. 6. Strain-free lattice parameter of austenite in AIM1 carburized at 500 °C for 1000 h.

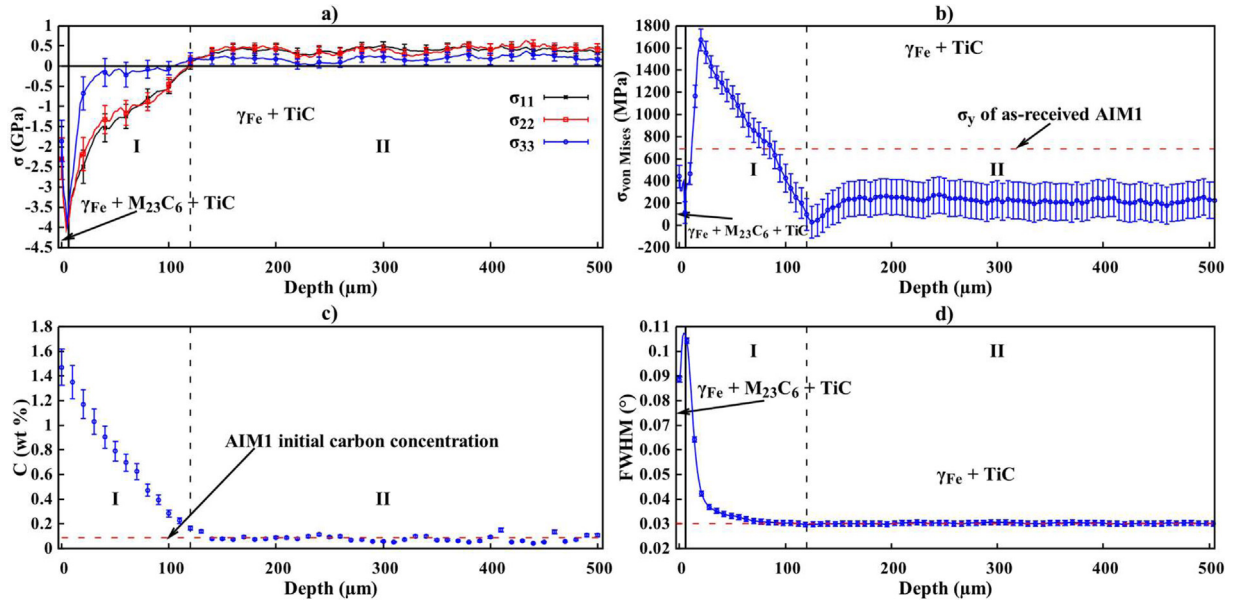


Fig. 7. AIM1 alloy carburized at 500 °C for 1000 h: a) Residual stress components in austenite, b) von Mises stress in austenite, c) Carbon concentration profile, d) FWHM of the austenite. The vertical continuous line indicates the zones depending on the formed phases. The vertical dashed line shows the limit of regions I and II.

the carbon concentration. For instance, for a carbon concentration equal to 1.4 wt.% which was the carbon concentration measured at the sample surface in our case, the yield stress was enhanced and reached 1.1 GPa [51]. The transition from compressive to tensile residual stress was the consequence of the mechanical equilibrium establishment (stress balance) in the whole sample. Different affected depths for the profiles of carbon, residual stress and FWHM were observed. Carbon diffused until 120 μm but generated a mechanical impact on a thicker region of 500 μm due to mechanical equilibrium establishment in the sample. The FWHM profile was differently affected: i) no evolution was observed in the non-carburized zone due to the absence of chemical gradient and plastic deformation and ii) an increase in the carburized region compared to the core of the material was measured due to the accumulation of plastic strains and chemical changes in that zone.

As already mentioned, the residual stress in AIM1 alloy carburized at 500 °C for 1000 h, presented in Fig. 10a, were calculated without taking into consideration the evolution of the XEC as function of carbon dissolved in austenite. That remains reasonable in our case. Jiang et al. [51] have mentioned a slight variation of the Young's modulus of a 316 L austenitic stainless steel between 195 GPa and 205 GPa for a variation of an amount of carbon dissolved in the austenite between 0.03 and 1.4 wt.%. This Young's modulus increase will induce a variation of 100 MPa in the value of residual stress calculated for the highest strain level which was about 3.5 GPa. This 100 MPa increase was lower than the experimental uncertainty given on this value. The cutting of the measured sample from the carburized plate can lead to residual stress relaxation. That effect was evaluated by FEM simulations using Cast3M software [52]. A stress relaxation due to sample cutting was observed but the residual stress profile within the depth of the sample was not affected. The maximum relaxation estimated by FEM simulation is about 25% occurring mainly in the beginning of the carburized zone and in the non-carburized zone from 200 μm to 500 μm. The point of zero stress marking the transition from compressive to tensile stress remains at the same depth and the relaxation at the vicinity of that point is less than in the rest of the sample (zero at the transition point). The stress relaxation was calculated only in the case of carburization at 500 °C. For car-

burization at 600 °C, the same relaxation mechanism could have occurred.

5.2. AIM1 alloy carburized at 600 °C for 1000 h

5.2.1. Strain-free lattice parameters of austenite and $M_{23}C_6$ carbide

The strain-free lattice parameter of austenite within the depth of the carburized sample was calculated as a function of its chemical composition using Eq. 6. The lattice expansion coefficient of carbon, $\alpha_C = 0.0405 \text{ \AA} / (\text{wt. \%}) C$, determined in section 5.1.1, was used. The chemical composition of austenite at any sample depth was predicted assuming local thermodynamic equilibrium of the carburized substrate. It was determined using Thermo-Calc® software at all measured carbon concentration. This methodology was presented and validated in a previous work [9].

The evolution of the austenite strain-free lattice parameter as a function of the sample depth is presented in Fig. 8. The austenite strain-free lattice parameter was not calculated in the region where M_7C_3 carbide formed. This was due to a disagreement between the experimental and predicted results from Thermo-Calc® in that region [9]. The strain-free lattice parameter was lower than the initial lattice parameter of AIM1, in agreement with the formation of chromium and molybdenum rich carbides which resulted in the depletion of these elements in austenite. More discussion on the effect of carbide formation on the lattice parameter of austenite were given in a previous article [9].

The evolution of the $M_{23}C_6$ strain-free lattice parameter as a function of the sample depth is presented in Fig. 9. It was not calculated in the region where M_7C_3 carbide formed for the same reason as the one given previously for austenite.

5.2.2. Residual stress in austenite

Fig. 10a, b, c and d show the evolution of the normal residual stress components, the von Mises stress, the evolution of the phases mass fractions and the FWHM of austenite in AIM1 alloy carburized at 600 °C for 1000 h. Two different evolution of the residual stresses were observed below the $M_7C_3 - M_{23}C_6$ carbide rich region where the residual stresses evolution could not be determined (Fig. 10a). First, the residual stresses increased with increasing depth and reached a maximum value at a depth around

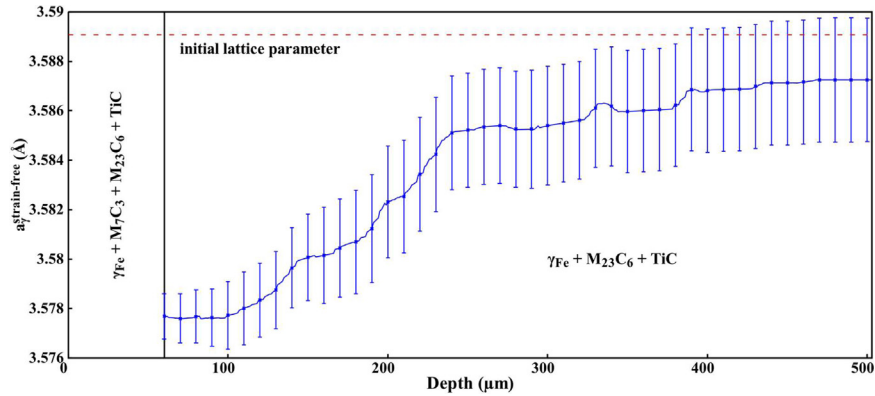


Fig. 8. Strain-free lattice parameter of austenite in AIM1 carburized at 600 °C for 1000 h.

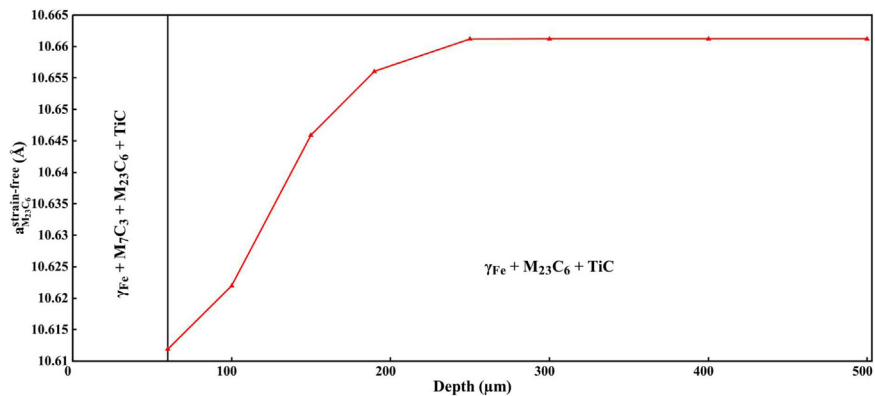


Fig. 9. Strain-free lattice parameter of $M_{23}C_6$ in AIM1 carburized at 600 °C for 1000 h.

180 μm . Then, the residual stresses decreased up to the center of the sample. Interestingly, the $M_{23}C_6$ fraction decreased with depth monotonously in both regions. Besides, the von Mises stresses (Fig. 10b) were lower than the tensile yield stress of as received AIM1 alloy (690 MPa) at any depth. An increase of the FWHM was observed at a depth of 220 μm . It increased until 120 μm in depth and reached a maximum value of $0.043 \pm 0.001^\circ$ against a value of $0.030 \pm 0.001^\circ$ in the core. Then, a slight decrease accompanied with a stabilization at a value of $0.040 \pm 0.001^\circ$ was observed.

It is proposed that the residual stress increase observed simultaneously with the $M_{23}C_6$ mass fraction increase from the center of the sample to 180 μm in depth was the consequence of the rise in elastic energy due to the elastic accommodation of the misfit between austenite and carbides lattices. In that region, carbides mainly formed in the grain boundaries of austenite (Figure 1 in supplementary materials). It was reported in literature that $M_{23}C_6$ carbide precipitating at austenite grain boundaries usually possesses coherent interface and orientation relationship with the austenite grain from which it precipitates [53–56]. So, the increase of the residual stress in the zone between the center of the sample and 180 μm could be justified by the increase of the amount of $M_{23}C_6$ precipitates in grain boundaries. From 180 to 60 μm in depth, the intermediate zone and the intragranular zone (see Fig. 1 in supplementary materials), and very likely in the region near the surface, a residual stress relaxation occurred whereas the $M_{23}C_6$ mass fraction still increased. That residual stresses relaxation could be explained by a loss of coherency between the austenite matrix and the $M_{23}C_6$ precipitates which resulted in a drop of the elastic energy and, as a consequence, a decrease of the residual stresses. Wen et al. [55] and Ding et al. [53] reported that $M_{23}C_6$ starts precipitation at the grain boundary from an austenite grain with which it is in coherence then,

grows fast into the interior of an adjacent grain without coherency forming curved incoherent interfaces. The same growth morphology was observed in the studied carburized samples. In Fig. 11, carbides precipitating from an austenite grain then growing in the adjacent grain forming curved incoherent interface are showed by red arrows. It was also reported that $M_{23}C_6$ carbides precipitating within the grains are incoherent with the matrix [54]. Moreover, Lewis and Hattersley [56] mentioned that $M_{23}C_6$ particles are never fully coherent with the matrix. Going towards the sample surface, the $M_{23}C_6$ mass fraction increased, the coarsening of the precipitates at the grain boundaries was observed and carbides were formed within the grains (see Fig. 11 and Figure 1 in supplementary materials). In consequence, the surface of incoherent interfaces increased. This phenomenon could be the principal reason of the observed residual stress relaxation. In short, the increase of the intragranular $M_{23}C_6$ carbides fraction in the sample decreases the value of the residual stresses created in austenite. The FWHM increase compared to the core material can be explained by: i) a chemical gradient (a profile of austenite depletion in chromium and molybdenum due to the formation of carbides) and ii) strain heterogeneities (massive presence of carbide in grains and at grain boundaries). It is important to highlight that the residual stress in austenite were tensile along the whole measured zone. These tensile stresses were the consequence of volume reduction in austenite due to depletion in carbide former elements, mainly chromium and molybdenum.

5.2.3. Residual stress in $M_{23}C_6$ carbide

Fig. 12 shows the residual stress in $M_{23}C_6$ within the depth of AIM1 carburized at 600 °C for 1000 h. Compressive residual stresses were developed in $M_{23}C_6$ carbide along the investigated depth range. The higher stress value, $\approx -4.2 \pm 0.1$ GPa,

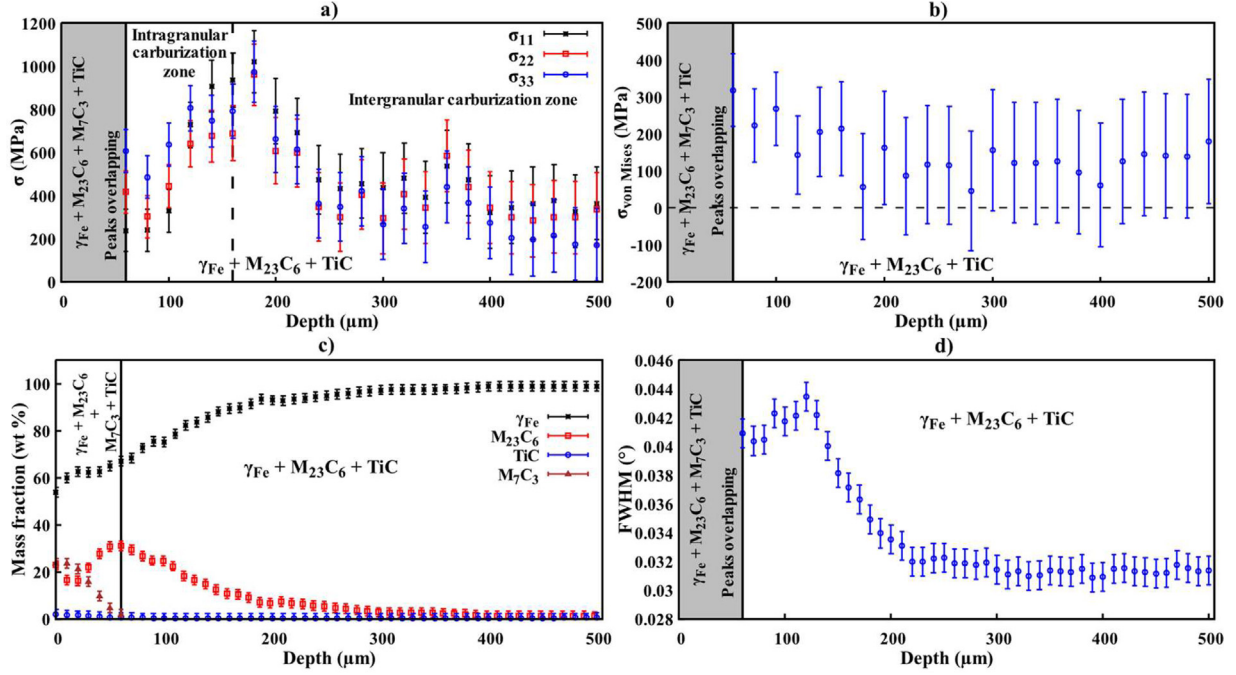


Fig. 10. AIM1 alloy carburized at 600 °C: a) Residual stress components in austenite, b) von Mises stress in austenite, c) Mass fractions of the diffracted phases, d) FWHM of the austenite.

was observed at 60 μm in depth below the $M_7C_3 - M_{23}C_6$ carbide rich region. Then, it decreased to reach a minimum value, $\approx -1.6 \pm 0.1$ GPa, at around 100 μm in depth. Deeper, the residual stresses increased again to reach a maximum value $\approx -3.3 \pm 0.17$ GPa around 250 μm in depth. In the rest of the sample, the residual stress determination was limited due to the not well-defined peaks of $M_{23}C_6$ carbide (small intensity/background ratio, $M_{23}C_6$ mass fraction lower than 2 wt.%). The residual stresses in $M_{23}C_6$ (Fig. 12) were calculated without taking into consideration the evolution of the XEC as function of the composition of $M_{23}C_6$. Gong et al. [57] have reported a chemical composition dependent evolution of $M_{23}C_6$ elasticity constants. Unfortunately, the data given in their study did not cover all the composition range and could not be used in our study. To carry out a real quantitative determination of the residual stresses in $M_{23}C_6$ carbide required supplementary input data which were not currently available.

5.2.4. Macroscopic residual stress

The macroscopic residual stresses developed in AIM1 carburized at 600 °C for 1000 h were calculated using Eq. (8) from the

residual stress profile determined in austenite and $M_{23}C_6$ carbides in the previous sections. It is shown in Fig. 13.

$$\sigma_{Macro} = f_v^{austenite} \sigma_{austenite} + f_v^{M_{23}C_6} \sigma_{M_{23}C_6} \quad (8)$$

with f_v^x and σ^x the volume fraction and the residual stress in the phase x respectively.

As explained previously, the macroscopic residual stress profile could not be determined in the nearest region of the surface where M_7C_3 formed. Underneath this region, the macroscopic residual stresses are compressive over 100 μm in depth. Deeper, macroscopic tensile stresses were formed. The higher tensile stress value was lower than the tensile yield stress of the carburized sample determined through tensile tests at room temperature (≈ 990 MPa) [3]. The residual stresses in the first 60 μm of depth which were not experimentally determined were very likely in compression in order to satisfy the macroscopic stress balance within the whole sample. A stress relaxation could be also expected at the extreme free surface of the sample. The chemically affected depth in the sample covered the whole sample generating residual stresses due to the depletion of austenite, the formation of carbides and me-

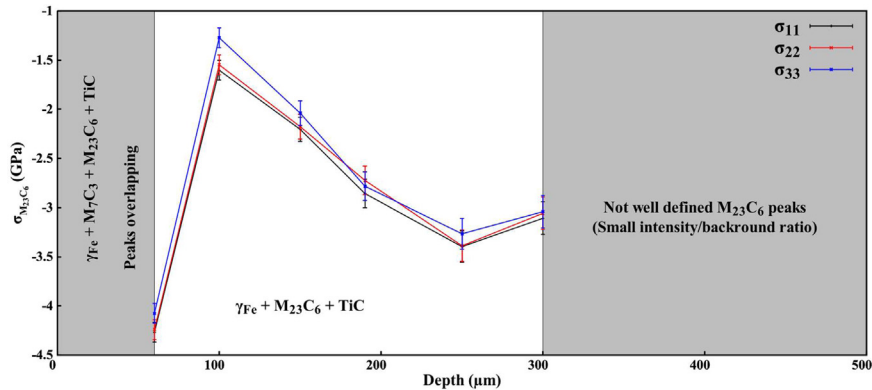


Fig. 12. $M_{23}C_6$ residual stress evolution within the depth of AIM1 carburized at 600 °C for 1000 h.

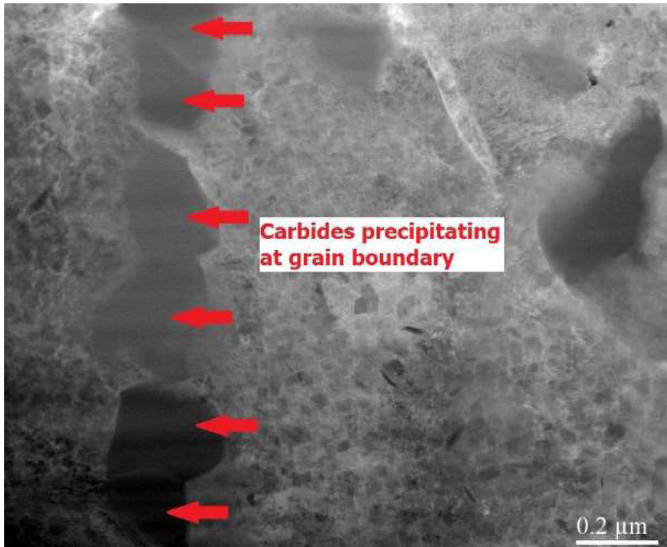


Fig. 11. TEM Annular Dark-Field micrograph of the lamella extracted at 100 μm from the surface of the AIM1 alloy carburized at 600 $^{\circ}\text{C}$ for 1000 h. Red arrows: M_{23}C_6 carbides precipitating at the grain boundary and growing into the interior of the grain.

chanical equilibrium establishment. Carburization at 600 $^{\circ}\text{C}$ does not generate plastic strain but created a chemical gradient and strain heterogeneities in about the first 200 μm of thickness resulting in the increase of the FWHM of austenite in that region.

It should be mentioned that the quantitative residual stress profiles determined in austenite and M_{23}C_6 carbide in that study were directly dependent on the calculated strain-free lattice parameters, hence on the expansion coefficient values and ab-initio data used in Eq. (6) and Eq. (7). Any variation within the uncertainty range given on the data cited previously would result in a variation of the calculated stresses in the range delimited by the error bars and will not in any case change the residual stress profile.

6. Conclusion

Residual stress gradients within the depth of a Ti-stabilized stainless steel cladding candidate after exposure to carburizing nuclear liquid sodium was measured with a micrometric depth resolution by high-energy X-ray diffraction.

- At 500 $^{\circ}\text{C}$, massive supersaturation of carbon in austenite mainly occurred. The expansion of the austenite cell due to dissolution of carbon resulted in the development of compressive residual stress in the carburized zone and tensile residual

stress in the non-carburized region. Plastic deformation might have occurred within the first 100 μm of depth. The value of the carbon expansion coefficient, α_{C} , was assessed based on the macroscopic stress balance assumption in the sample.

- At 600 $^{\circ}\text{C}$, chromium carbides mainly formed as carbon diffused in the sample. Tensile and compressive residual stresses were developed in austenite and M_{23}C_6 respectively. The degree of residual stress developed in austenite was dependent on the M_{23}C_6 mass fraction and the coherence between the matrix and the precipitates. A relaxation of the residual stress in austenite was observed in the intragranular carburization zone. In that zone, the carbides precipitate without coherency with the austenitic matrix. The macroscopic residual stresses were compressive in the carburized zone and tensile in the rest of the sample. No plastic deformation was observed at this carburization temperature.

Funding

This work was supported by the French Alternative Energies and Atomic Energy Commission, EDF, Framatome, the project CALIPSOplus under the Grant Agreement 730,872 from the EU Framework Programme for Research and Innovation HORIZON 2020 and the French State through the program "Investment in the future" operated by the National Research Agency (ANR) and referenced by ANR-11-LABX-0008-01 [58].

Declaration of Competing Interest

The authors declare that they have no known competing financial interests or personal relationships that could have appeared to influence the work reported in this paper.

Acknowledgments

The authors gratefully acknowledge the Deutsches Elektronen-Synchrotron (DESY-Petra III, Hamburg, Germany) for provision of beamtime at the PETRA P07-EH2 beamline. We would like to thank Olof Gutowski for assistance during the experiments and Professor Dominique Poquillon for the FE simulations. The RG4 project from CEA is thanked for having partially funded this study.

Supplementary materials

Supplementary material associated with this article can be found, in the online version, at doi:10.1016/j.actamat.2021.117435.

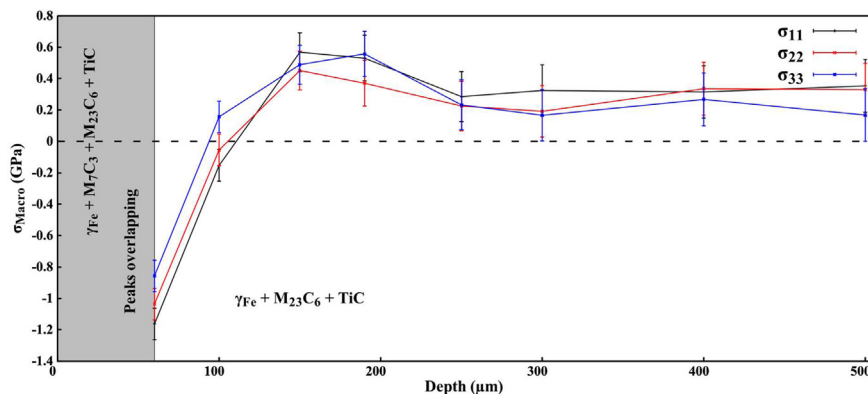


Fig. 13. Macroscopic residual stress in AIM1 carburized at 600 $^{\circ}\text{C}$ for 1000 h.

References

- [1] A. Throley, C. Tyzack, The carburization of stainless steels in sodium containing carbon impurities and its effect on mechanical properties, Effects of environment on material properties in nuclear systems (1971). doi:10.1680/eoempins.44579.0015.
- [2] J.L. Krankota, The effect of carburization in sodium on the mechanical properties of stainless steels, *J. Eng. Mater. Technol.* 98 (1) (1976) 9–16.
- [3] F. Rouillard, Influence de la carburation sur le comportement mécanique des aciers : données d'entrée pour la loi de durée de vie des gaines des, *Éléments Absorbants et Réflexions* (2017) NT DPC/SCCME 18-872-A.
- [4] W.F. Holcomb, Carburization of type 304 stainless steel in liquid sodium, *Nucl. Eng. Des.* 6 (1967) 264–272.
- [5] F.B. Litton, A.E. Morris, Carburization of type 316 L stainless steel in static sodium, *J. Less-Common Met.* 22 (1970) 71–82.
- [6] N. Sivai Baharasi, K. Thyagarajan, H. Shaikh, M. Radhika, A.K. Balamurugan, S. Venugopal, A. Moitra, S. Kalavathy, S. Chandramouli, A.K. Tyagi, R.K. Dayal, K.K. Rajan, Evaluation of microstructural, mechanical properties and corrosion behavior of AISI type 316LN stainless steel and modified 9Cr-1Mo steel exposed in a dynamic bimetallic sodium loop at 798 K (525 °C) for 16 000 h, *Metall. Mater. Trans. A* 43A (2012) 561–571.
- [7] N. Sivai Baharasi, M.G. Pujar, K. Thyagarajan, C. Mallika, U. Kamachi Mudali, A. Dhul, M. Nandagopal, A. Moitra, S. Chandramouli, K.K. Rajan, Changes in microstructural and mechanical properties of AISI type 316LN stainless steel modified 9Cr-1Mo steel on long-term exposure to flowing sodium in a bi-metallic loop, *Metall. Mater. Trans. A* 46A (2015) 6065–6080.
- [8] M. Romedenne, F. Rouillard, D. Hamon, B. Malard, D. Monceau, Carburization of austenitic and ferritic stainless steels in liquid sodium: comparison between experimental observations and simulations, *Corrosion Sci.* 159 (2019) 108147.
- [9] M.F. Slim, G. Geandier, B. Malard, F. Rouillard, Microstructural and chemical changes of a Ti-stabilized austenitic stainless steel after exposure to liquid sodium at temperatures between 500 °C and 650 °C, *Metall. Mater. Trans. A* (2021), doi:10.1007/s11661-021-06396-1.
- [10] M.F. Slim, G. Geandier, M. Romedenne, F. Rouillard, B. Malard, Carburization and stress profiles characterized by high-energy x-ray diffraction in 316 L austenitic stainless steel after exposure at 500 °C and 600 °C in carburizing liquid sodium, *Oxid. Met.* (2021), doi:10.1007/s11085-021-10039-6.
- [11] J. Keckes, M. Bartosik, C. Mitterer, R. Daniel, G. Maier, W. Ecker, J. Vila-Comamala, C. David, S. Schoeder, M. Burghammer, X-ray nanodiffraction reveals strain and microstructure evolution in nanocrystalline thin films, *Scr. Mater.* 67 (2012) 748–751.
- [12] S.J.B. Kurz, S.R. Meka, N. Schell, W. Ecker, J. Keckes, E.J. Mittemeijer, Residual stress and microstructure depth gradients in nitride iron-based alloys revealed by dynamical cross-sectional transmission X-ray microdiffraction, *Acta Mater.* 87 (2015) 100–110.
- [13] J. Todt, H. Hammer, B. Sartory, M. Burghammer, J. Kraft, R. Daniel, J. Keckes, S. Defregger, X-ray nanodiffraction analysis of stress oscillations in a W thin film; on through-silicon via, *J. Appl. Crystallogr.* 49 (2016) 182–187.
- [14] J. Todt, C. Krywka, Z.L. Zhang, P.H. Mayrhofer, J. Keckes, M. Bartosik, Indentation response of a superlattice thin film revealed by in-situ scanning X-ray nanodiffraction, *Acta Mater.* 195 (2020) 425–432.
- [15] J. Keckes, R. Daniel, J. Todt, J. Zalesak, B. Sartory, S. Braun, J. Gluch, M. Rosenthal, M. Burghammer, C. Mitterer, S. Niese, A. Kubec, 30 nm X-ray focusing correlates oscillatory stress, texture and structural defect gradients across multilayered TiN-SiO₂ thin film, *Acta Mater.* 144 (2018) 862–873.
- [16] M. Romedenne, F. Rouillard, B. Duprey, D. Hamon, M. Tabarant, D. Monceau, Carburization of austenitic and ferritic steels in carbon-saturated sodium: preliminary results on the diffusion coefficient of carbon at 873 K, *Oxid. Met.* 87 (2017) 643–653.
- [17] M. Romedenne, Etude De La Carburation Et De Boruration D'aciers Inoxydables En Milieu sodium: Interaction B₄C – Gaine, Thèse de doctorat de l'Université de Toulouse, 2018.
- [18] J. Kieffer, D. Karkoulis, PyFAI, a versatile library for azimuthal regrouping, *J. Phys. Conf. Ser.* 425 (2013) 202012.
- [19] L. Lutterotti, S. Matthies, H.R. Wenk, MAUD (Material Analysis using Diffraction): a user-friendly java program for Rietveld texture analysis and more, in: *Proceeding of the 12th International Conference on Textures of Materials (ICOTOM-12)*, 1, 1999, p. 1599.
- [20] C. Le Boulrot, Caractérisation de l'hétérogénéité du champ des déformations élastiques dans les matériaux polycristallins par diffraction des rayons X et des neutrons – application à un acier duplex, Ph. D. Thesis, Université de Paris, France (2012).
- [21] G. Geandier, L. Vautrot, B. Denand, S. Denis, In situ stress determination during phase transformation of a metal matrix composite by High-Energy X-ray Diffraction, *Materials (Basel)* 11 (2018) 1415.
- [22] I. Noyan, J. Cohen, *Residual Stress Measurement By Diffraction and Interpretation*, Springer Verlag, New York, 1987.
- [23] V. Hauk, *Structural and Residual stress Analysis By Nondestructive Methods*, Elsevier, Amsterdam, 1997.
- [24] M. Gelfi, E. Bontempi, R. Roberti, L.E. Depero, X-ray diffraction Debye Ring Analysis for Stress measurement (DRAST): a new method to evaluate residual stresses, *Acta Mater.* 52 (2004) 583–589.
- [25] F. Heidelbach, C. Riekel, H.R. Wenk, Quantitative texture analysis of small domains with synchrotron radiation X-rays, *J. Appl. Crystallogr.* 32 (1999) 841–849.
- [26] B. Clausen, T. Lorentzen, T. Leffers, Self-consistent modelling of the plastic deformation of F.C.C polycrystals and its implications for diffraction measurements of internal stresses, *Acta Mater.* 46 (1998) 3087–3098.
- [27] C. Jiang, First-principles study of structural, elastic, and electronic properties of chromium carbides, *Appl. Phys. Lett.* 92 (2008) 041909.
- [28] R. Hill, The elastic behavior of a crystalline aggregate, *Proceedings of the Physical Society A* 65 (1952) 349–354.
- [29] JCGM 100: Evaluation of measurement data - Guide to the expression of uncertainty in measurement (2008).
- [30] JCGM 200: international vocabulary of metrology - Basic and general concepts and associated terms (VIM) (2012).
- [31] P.J. Withers, M. Preuss, A. Steuwer, J.W.L. Pang, Methods for obtaining the strain-free lattice parameter when using diffraction to determine residual stress, *J. Appl. Crystallogr.* 40 (2007) 891–904.
- [32] D.J. Dyson, B. Holmes, Effect of alloying additions on the lattice parameter of austenite, *J. Iron and Steel Institute* 208 (1970) 469–474.
- [33] Y. Cao, F. Ernst, G.M. Michal, Colossal carbon supersaturation in austenitic stainless steels carburized at low temperature, *Acta Mater.* 51 (2003) 4171–4181.
- [34] Y. Sun, X. Li, T. Bell, Structural characteristics of low temperature plasma carburized austenitic stainless steel, *Mater. Sci. Technol.* 15 (1999) 1171–1178.
- [35] H. Kahn, G.M. Michal, F. Ernst, A.H. Heuer, Poisson effects on X-ray diffraction patterns in low-temperature-carburized austenitic stainless steel, *Metall. Mater. Trans. A* 40A (2009) 1799–1804.
- [36] L. Cheng, A. Böttger, Th.H.de Keijser, E.J. Mittemeijer, Lattice parameters of iron-carbon and iron-nitrogen martensites and austenites, *Scr. Metall. Mater.* 24 (1990) 509–514.
- [37] C.P. Scott, J. Drillet, A study of the carbon distribution in retained austenite, *Scr. Mater.* 56 (2007) 489–492.
- [38] T.S. Hummelshoj, T.L. Christiansen, M.A.J. Somers, Lattice expansion of carbon-stabilized expanded austenite, *Scr. Mater.* 63 (2010) 761–763.
- [39] N.H. van Dijk, A.M. Butt, L. Zhao, J. Sietsma, S.E. Offerman, J.P. Wright, S. van der Zwaag, Thermal stability of retained austenite in TRIP steels studied by synchrotron X-ray diffraction during cooling, *Acta Mater.* 53 (2005) 5439–5447.
- [40] S.J. Lee, Y.K. Lee, Quantitative analyses of ferrite lattice parameter and solute Nb content in low carbon microalloyed steels, *Scr. Mater.* 52 (2005) 973–976.
- [41] Y. Yijie, X. Weiwei, X. Fangfang, G. Tieqiang, C. Lijie, Effects of alloying elements M (M = Fe, Mo) on phase stability of Cr₂₃C₆ carbides from first principles, *Adv. Eng. Res.* 121 (2017).
- [42] A.L. Bowman, G.P. Arnold, E.K. Storms, N.G. Nereson, The crystal structure of Cr₂₃C₆, *Acta Crystallographica B* B28 (1972) 3102–3103.
- [43] F. Ernst, Y. Cao, G.M. Michal, Carbides in low-temperature-carburized stainless steels, *Acta Mater.* (2004) 1469–1477.
- [44] T. Christiansen, M.A.J. Somers, Stress and composition of carbon stabilized expanded austenite on stainless steel, *Metall. Mater. Trans. A* 40A (2009) 1791–1798.
- [45] T.L. Christiansen, T.S. Hummelshoj, M.A.J. Somers, Expanded austenite, crystallography and residual stress, *Surf. Eng.* 26 (2010) 242–247.
- [46] Y. Peng, Z. Liu, Y. Jiang, B. Wang, J. Gong, M.A.J. Somers, Experimental and numerical analysis of residual stress in carbon-stabilized expanded austenite, *Scr. Mater.* 157 (2018) 106–109.
- [47] D. Hoefl, B.A. Latella, K.T. Short, Residual stress and cracking in expanded austenite layers, *J. Phys. Condens. Matter* 17 (2005) 3547–3558.
- [48] S. Jegou, T.L. Christiansen, M. Klaus, Ch. Genzel, M.A.J. Somers, Determination of composition, residual stress and stacking fault depth profiles in expanded austenite with energy-dispersive diffraction, *Thin Solid Films* 530 (2013) 71–76.
- [49] F.A.P. Fernandes, T.L. Christiansen, G. Winter, M.A.J. Somers, On the determination of stress profiles in expanded austenite by grazing incidence X-ray diffraction and successive layer removal, *Acta Mater.* 94 (2015) 271–280.
- [50] P.J. Withers, in: *Residual stresses: Measurement by Diffraction*, Encyclopedia of Materials: Science and Technology, 2001, pp. 8158–8170.
- [51] Y. Jiang, Q. Wu, Y. Li, Y. Peng, J. Gong, Mechanical properties of low-temperature gaseous carburized layer in 316 L stainless steel based on nano-indentation and four-point bending tests, 387, 125501 (2020).
- [52] <http://www-cast3m.cea.fr>.
- [53] Z. Ding, B. Liang, Z. Xu, L. Dong, Multiple interface structures of M₂₃C₆ carbides at grain boundary in an aged 100Mn13 high carbon high manganese steel, *Am. Chem. Society Appl. Mater. Interfaces* 12 (2020) 19235–19242.
- [54] Z. Xu, Z. Ding, L. Dong, B. Liang, Characterization of M₂₃C₆ carbides precipitating at grain boundaries in 100Mn13 steel, *Metall. Mater. Trans. A* 47A (2016) 4862–4868.
- [55] H. Wen, B. Zhao, X. Dong, F. Sun, L. Zhang, Preferential growth of coherent precipitates at grain boundary, *Mater. Lett.* 261 (2020) 126984.
- [56] M.H. Lewis, B. Hattersley, Precipitation of M₂₃C₆ in austenitic steels, *Acta Metall.* 13 (1965) 1159–1168.
- [57] X. Gong, C. Cui, Q. Yu, W. Wang, W. Xu, L. Chen, First-principles study of phase stability and temperature-dependent mechanical properties of (Cr, M)₂₃C₆ (M = Fe, Mo) phases, *J. Alloys Compd.* 824 (2020) 153948.
- [58] LabEx DAMAS. Available online: labex-damas.univ-lorraine.fr.